



Suprathermal H⁺ Pickup Ion Tails in the Outer Heliosphere

Bishwas L. Shrestha¹ , Eric J. Zirnstein¹ , David J. McComas¹ , Pontus Brandt² , Alan Stern³ , Heather A. Elliott⁴ ,
Andrew R. Poppe⁵ , Kelsi N. Singer³ , and Anne Verbiscer^{6,7}

¹ Department of Astrophysical Sciences, Princeton University, Princeton, NJ 08544, USA; bishwasls@princeton.edu

² The Johns Hopkins University Applied Physics Laboratory, Laurel, MD 20723, USA

³ Southwest Research Institute, Boulder, CO, USA

⁴ Southwest Research Institute, San Antonio, TX, USA

⁵ Space Sciences Laboratory, University of California, Berkeley, CA 94720, USA

⁶ University of Virginia, Charlottesville, VA, USA

Received 2023 September 20; revised 2023 October 29; accepted 2023 October 31; published 2023 December 20

Abstract

This study provides a detailed analysis of five distant interplanetary shocks observed by the Solar Wind Around Pluto instrument on board New Horizons, which exhibit the signature of a suprathermal H⁺ pickup ion (PUI) tail in the downstream distribution. These shocks were observed with a PUI data cadence of approximately 24 hr, covering a heliocentric distance range of 23.71–36.75 au. The shock compression ratio varies between approximately 1.4 and 3.2. The H⁺ PUI density and temperature show a gradual increase across the shock, while the H⁺ solar wind density shows erratic behavior without a distinct downstream compression. The H⁺ PUI cooling index variation across the shock displays different characteristics in each shock. This study demonstrates, for the first time, the variation of the number density of downstream H⁺ PUI tails with the shock compression ratio, revealing an increase in tail density with stronger shocks. Additionally, theoretical estimates of reflected PUI number densities derived from the electrostatic cross-shock potential agree very well with the observed H⁺ PUI tail densities for stronger shocks.

Unified Astronomy Thesaurus concepts: [Interplanetary shocks \(829\)](#); [Pickup ions \(1239\)](#); [Solar wind \(1534\)](#); [Heliosphere \(711\)](#); [Interplanetary particle acceleration \(826\)](#); [Space plasmas \(1544\)](#); [Plasma physics \(2089\)](#)

1. Introduction

Interstellar pickup ions (PUIs) are created by the ionization of the interstellar neutral (ISN) atoms through charge exchange, photoionization, and electron impact ionization in the heliosphere. Once created, they are picked up by the motional electric field of the solar wind (SW) flow and gyrate around the interplanetary magnetic field to form a ring beam distribution (Zirnstein et al. 2022). The newly formed PUIs are picked up by the motional electric field of the SW with a velocity equivalent to the difference between the bulk SW velocity and the interstellar atom velocity. The PUI ring beam is unstable and experiences pitch angle scattering and isotropization by either ambient and/or self-generated low-frequency electromagnetic fluctuations to form a shell distribution. PUIs comove with the bulk SW (thus, the term *pickup*), experiencing a nonadiabatic cooling (McComas et al. 2021) with increasing heliocentric distance, and consequently form a filled-shell distribution (Vasyliunas & Siscoe 1976). The filled-shell distribution contains the freshly injected PUIs at the outermost layer, while the PUIs formed close to the Sun populate progressively more inner layer. PUIs are not thermalized with the SW because the Coulomb collision timescale for protons is significantly larger than the SW propagation time (Isenberg 1986).

The Solar Wind Around Pluto (SWAP) instrument on New Horizons detects ions in the energy range of ~ 0.021 – 7.8 keV q^{-1} (McComas et al. 2008) and has provided unprecedented measurements of H⁺ PUIs from ~ 10 au out to ~ 52.5 au from the Sun (Randol et al. 2012, 2013; Swaczyna et al. 2020; McComas et al. 2021, 2022). The SWAP instrument remains operational on New Horizons, and is currently at ~ 57 au from the Sun. McComas et al. (2017) computed the moment-like H⁺ PUI parameters by fitting a classic Vasyliunas & Siscoe (1976) model to the observed SWAP count rates from ~ 22 – 38 au and showed that H⁺ PUIs dominate the internal pressure in the outer heliosphere, beyond ~ 20 au. Though their model fits were generally adequate, the best-fit values of fitting parameters such as local ionization rate and ionization cavity size were often unphysically large or small. Swaczyna et al. (2020) reanalyzed the H⁺ PUI observations provided by McComas et al. (2017) by incorporating a nonadiabatic cooling index for H⁺ PUI fitting using the Chen et al. (2014) model to derive the interstellar neutral H density. They showed that the interstellar neutral hydrogen density in the vicinity of the heliosphere is much larger ($\sim 40\%$ larger) than the previously accepted consensus value (Bzowski et al. 2009). McComas et al. (2021) extended the PUI observations out to ~ 46.6 au from the Sun with improved analysis incorporating the nonadiabatic cooling index (Chen et al. 2014; Swaczyna et al. 2020) as free parameters. They found that the daily averaged PUI distribution beyond ~ 22 au shows additional heating of PUIs above the adiabatic cooling. In addition, they used superposed epoch analysis to examine the *average behavior* of 39 interplanetary shocks over that interval.

The first detailed study of an interplanetary shock with SWAP data was performed by Zirnstein et al. (2018), where they examined a strong shock at ~ 34 au from the Sun. They found that H⁺ PUIs are preferentially heated across the shock

⁷ The New Horizons SWAP Team.

compared to SW protons. Their study also shows the development of high-energy H^+ PUI tail downstream of the interplanetary shock that accounted for $\sim 20\%$ of the total downstream energy flux. McComas et al. (2022) presented a detailed analysis of seven distant interplanetary shock waves (six forward and one reverse shock) observed by SWAP from 49.5–52 au using newly available, hi-cadence (~ 30 minute resolution) data. Their study was able to resolve the shock transitions at distant interplanetary shocks for the first time. Their study also verified the preferential heating of PUIs across distant interplanetary shocks. Additionally, PUIs are likely preferentially heated at the heliospheric termination shock (HTS; Lee et al. 1996; Zank et al. 1996; Mostafavi et al. 2018) and believed to be the primary source of ~ 0.5 –7 keV ions in the inner heliosheath (Zank et al. 2010; Shrestha et al. 2020; Zirnstein et al. 2021; Baliukin et al. 2022; Gkioulidou et al. 2022; Kornbleuth et al. 2023), the region between the HTS and heliopause. Consequently, PUIs are critical to the force balance in the heliosheath (Decker et al. 2008; Dialynas et al. 2020) and constitute the parent population of many energetic neutral atoms (ENAs) created beyond the HTS that are being observed by NASA’s Interstellar Boundary Explorer (IBEX; McComas et al. 2009) and have been observed by Cassini (Krimigis et al. 2009).

The mechanism of PUI heating at distant interplanetary shocks and the formation of a suprathermal PUI tail is not well understood. Many physical processes are believed to be responsible for this, such as the reflection of ions from the electrostatic cross-shock potential (Lee et al. 1996; Zank et al. 1996) or magnetic deflections (Leroy 1983) or reflection in contracting and reconnecting magnetic islands (Drake et al. 2013), shock drift acceleration (SDA), diffusive shock acceleration (DSA), damping of MHD waves (Le Roux & Ptuskin 1998), etc. A dominant energy dissipation mechanism at the quasi-perpendicular shocks is the reflection of incident ions by the electrostatic cross-shock potential (CSP). The CSP is formed as a result of charge separation between ions and electrons across the shock. The reflected ions are trapped ahead of the shock ramp (called the foot) and gain energy from the upstream motional electric field, until the particle Lorentz force is large enough to overcome the electrostatic CSP barrier. Some ions can experience multiple reflections at the shock front and gain considerable energy. The multiply reflected PUI spectra can be approximated by a power-law distribution (Zank et al. 1996; Lipatov et al. 1998; Rice et al. 2001). Part of the reflected PUI population could be further accelerated by the DSA process (Wang et al. 2023) provided that the particle speed is above the injection energy. The injection problem in the theory of shock acceleration is still under debate (Giacalone & Jokipii 1999; Zank et al. 2001, 2006; Giacalone 2012; Giacalone et al. 2022; Perri et al. 2022). The downstream DSA particle distribution follows a power law, $f(v) \propto v^{-\gamma}$ (Lee et al. 2012; Zank 2014), where the power-law index (γ) depends on the shock compression ratio (r_c) as $\gamma = \frac{3r_c}{r_c - 1}$. Here, the shock compression ratio (r_c) is the ratio between the downstream and upstream plasma density.

In this study, we present a detailed analysis of the suprathermal H^+ PUI tail downstream of five distant interplanetary shocks observed by the SWAP instrument on New Horizons. These shocks are observed during the longer accumulation data (~ 24 hr cadence) over a heliocentric distance of 23.71–36.75 au. We analyze shocks with

compression ratios ranging from ~ 1.4 –3.2. We estimate the number density and effective temperature of suprathermal H^+ PUI tails by fitting a power-law distribution isotropic in the SW frame. We also show how the number density of the suprathermal H^+ PUI tail varies with the shock compression ratio. Finally, we compare these results with the theoretical estimate of the reflected PUI number density based on the theory of electrostatic CSP. The results of this study are also useful when characterizing the PUI heating mechanism downstream of the HTS and the subsequent formation of the ENAs.

2. Results and Discussions

We present a detailed analysis of five fast-forward shocks showing the signature of a suprathermal H^+ PUI tail in the downstream distribution observed by the SWAP instrument on board New Horizons. We use SW and PUI data collected by SWAP from 2012 July 20 to 2016 October 20 over a heliocentric distance between 23.71 and 36.75 au. The New Horizons spacecraft was moving with a heliocentric speed of ~ 14 km s^{-1} over this distance range. The PUI data used has a cadence of ~ 24 hr and is publicly available at https://spacephysics.princeton.edu/sites/g/files/toruqf1376/files/media/swap_pui_data_1.txt. Note that the PUI data used in this study was collected before the SWAP flight software update on 2021 February 19, which was performed to provide the hi-cadence measurement (~ 30 minute cadence) of PUIs. The H^+ SW data has a cadence of ~ 10 minutes, which is SWAP’s fine sweep data around the SW proton peak and is publicly available at <https://cdaweb.gsfc.nasa.gov/>. This study also includes a reanalysis of the strong interplanetary shock presented by Zirnstein et al. (2018) with an updated data processing method. See section 2.3 for details of the updated data processing used for the reanalysis of this shock.

2.1. Variation of PUI Properties across the Interplanetary Shock

A strong interplanetary shock S1 observed by SWAP at a radial distance of 23.77 au is shown in Figure 1. The top four panels represent the variation of H^+ SW properties and the bottom four panels represent the variation of H^+ PUI properties. The gray dots represent the SW properties from SWAP’s fine sweep data around the SW proton peak, whereas the black dots represent the SW and PUI properties from SWAP’s coarse sweep data. The results from both fine and coarse sweeps are shown for the SW but only the fine sweep results are used for the calculation of upstream and downstream quantities. The black-colored dashed vertical line represents the position of the shock, which is identified manually as a sharp jump in the SW speed. The shaded gray areas represent the upstream and downstream intervals of ~ 24 hr. Note that a single piece of data from the coarse histogram just before the shock is removed from this plot because the PUI distribution fit is extremely poor for highly anisotropic SWAP count rates observed during the shock transition.

The SW speed shows a $\sim 21\%$ jump from ~ 351.4 to 425.5 km s^{-1} , and a significant increase in the H^+ SW temperature ($\sim 166\%$) downstream of the shock. The H^+ PUI density and temperature show a gradual increase across the shock while the jump in the SW density is not apparent and shows an erratic behavior instead. Similar behavior of H^+ SW ions around

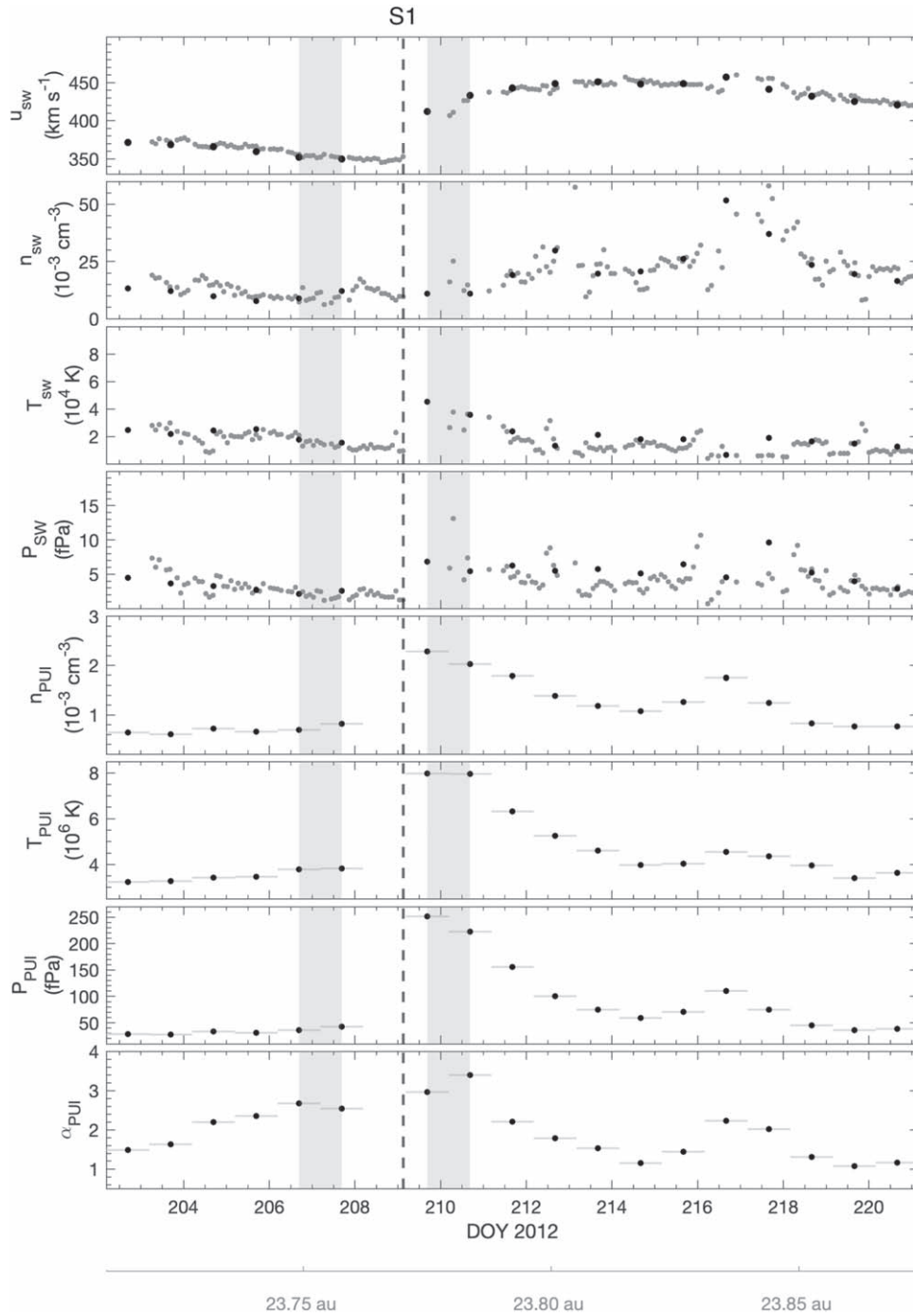


Figure 1. A strong interplanetary shock S1 observed by the SWAP instrument on New Horizons at ~ 23.8 au from the Sun. The top four panels represent the H^+ SW properties, while the bottom four panels represent the H^+ PUI properties. The dashed vertical black line marks the position of the shock while the shaded gray regions represent the upstream and downstream regions. The gray horizontal line along black data points on the bottom four panels represents the day-long time intervals over which PUI data were taken.

outer heliosphere shocks is also reported in previous Voyager (Richardson et al. 2008) and SWAP observations (Zirmstein et al. 2018; McComas et al. 2022). Part of the reason for the lack of significant correlation between SW density and speed might be because of the differential flow between core SW and PUI at the shock, also discussed in McComas et al. (2022). Ions can be deflected perpendicular to the magnetic field direction along the shock surface by the electrostatic cross-shock potential or magnetic deflection (Leroy 1983; Kumar et al. 2018). Because the PUIs have a velocity distribution with a larger thermal spread,

their bulk flow vector in the shock frame is less affected by the flow deflection compared to the core SW. This can result in a differential flow between core SW and PUIs across the shock. The relatively larger flow deflection at shocks could influence the measurement of the SW density by SWAP as it spins about the Earth-pointing axis. Another physical reason for the erratic behavior of SW could be that other SW structures, unrelated to the shock, are affecting the SW ions but not the daily averaged PUIs, possibly due to their vast difference in gyroradius. However, it is very difficult to characterize these fundamental

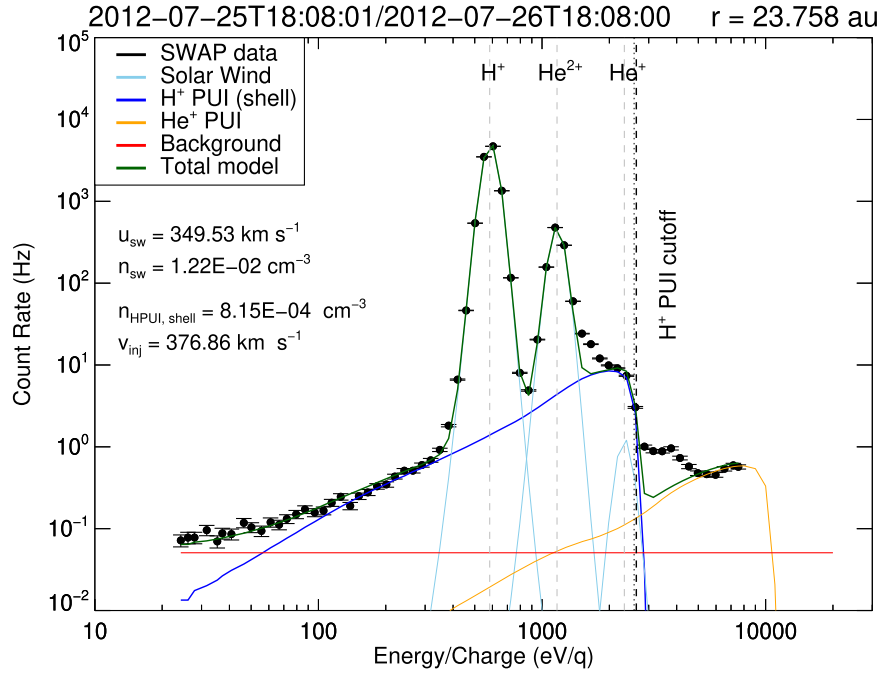


Figure 2. Daily averaged SWAP count rates in the spacecraft frame just before shock S1. Fitted SW proton (H^+), alpha particle (He^{2+}), and He^+ peaks are shown in light blue with centroids indicated by vertical dashed lines, and the fitted He^+ PUI is shown by the orange curve. These fits follow the same method described in McComas et al. (2021). The fitted H^+ PUI shell is shown by the dark blue curve which is taken directly from the result of McComas et al. (2021).

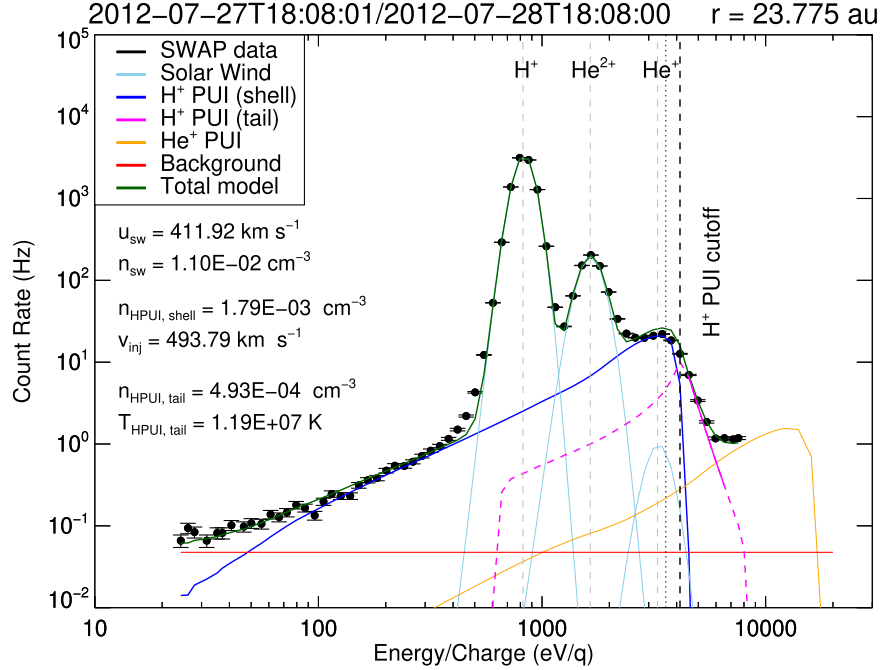


Figure 3. Daily averaged SWAP count rates in the spacecraft frame just after shock S1. Fits to the H^+ PUI tail are shown in the magenta-colored curve (see text for details). Fitted SW proton (H^+), alpha particle (He^{2+}), He^+ peaks, H^+ PUI shell, and the He^+ PUI have the same notation as in Figure 2.

processes with the one-dimensional E/q measurements from SWAP; thus, these are currently just conjectures that will be the subject of future studies. The upstream and downstream H^+ SW and PUI quantities are summarized in Table 2.

The PUI cooling index (α_{PUI}) is defined as $\left(\frac{v}{v_{inj}}\right)^{\alpha_{PUI}} = \left(\frac{r_{pickup}}{r}\right)$, where v is the PUI speed at the current distance r , and v_{inj} is the PUI injection speed at distance r_{pickup} , where the ion was picked up. The generalized filled-shell distribution function including the

nonadiabatic PUI cooling index is expressed as

$$f(r, w) = \frac{\alpha_{PUI} S(r, w)}{4 \pi r u_{SW} v_{inj}^3} w^{\alpha_{PUI}-3} n_{H, HTS} \times \exp\left(-\frac{\lambda}{r} \frac{\theta}{\sin \theta} w^{-\alpha_{PUI}}\right) \Theta(1-w), \quad (1)$$

where $S(r, w)$ is the survival probability of PUIs from their pickup distance to the point of observation, $w = v/v_{inj}$, u_{SW} is

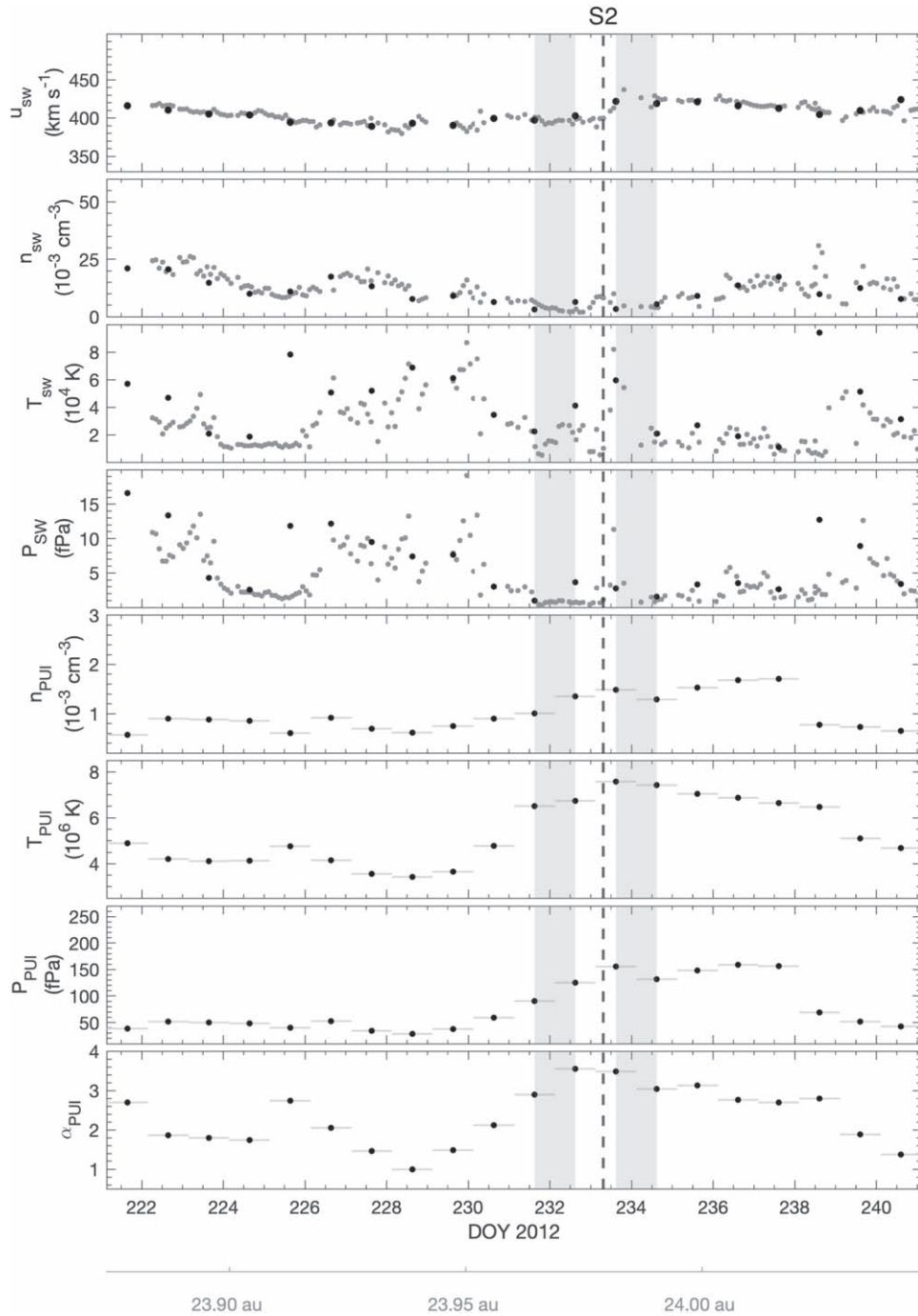


Figure 4. Variation of H^+ SW and H^+ PUI quantities across a relatively weak interplanetary shock S2 observed by SWAP at ~ 24.0 au from the Sun. The figure has the same notation as in Figure 1.

the local bulk SW speed in the solar frame, β_0 is the ionization rate normalized to the distance $r_0(1 \text{ au})$, $n_{H,HTS}$ is the interstellar neutral hydrogen density at the upwind HTS, θ is the angle between the SW flow direction and the interstellar flow direction, λ is the size of hydrogen ionization cavity, and Θ is the Heaviside step function.

Interestingly, the PUI cooling index (α_{PUI}) starts to increase ~ 1 week before the shock and reaches the adiabatic value ~ 1 week after the shock. This behavior is somewhat different from that reported by McComas et al. (2022) in the analysis of high-time resolution observations of relatively weaker shocks ($r_c < 2$). Their study shows that the cooling index increases

only ~ 1 week after the shock. McComas et al. (2021) also showed that the cooling index peaked a week after the shock passage, on average, in a superposed epoch analysis of 39 shocks. The different behavior of the cooling index across shock S1 is likely related to the presence of a suprathermal tail in the downstream H^+ PUI distribution. The cooling index only characterizes the heating of the shell part of the PUI distribution and cannot capture the suprathermal PUI tail part because they are created by a different acceleration mechanism. Note that the shocks analyzed in McComas et al. (2021, 2022) do not contain suprathermal H^+ PUI tails in the downstream distribution. Thus, whichever mechanism is creating the

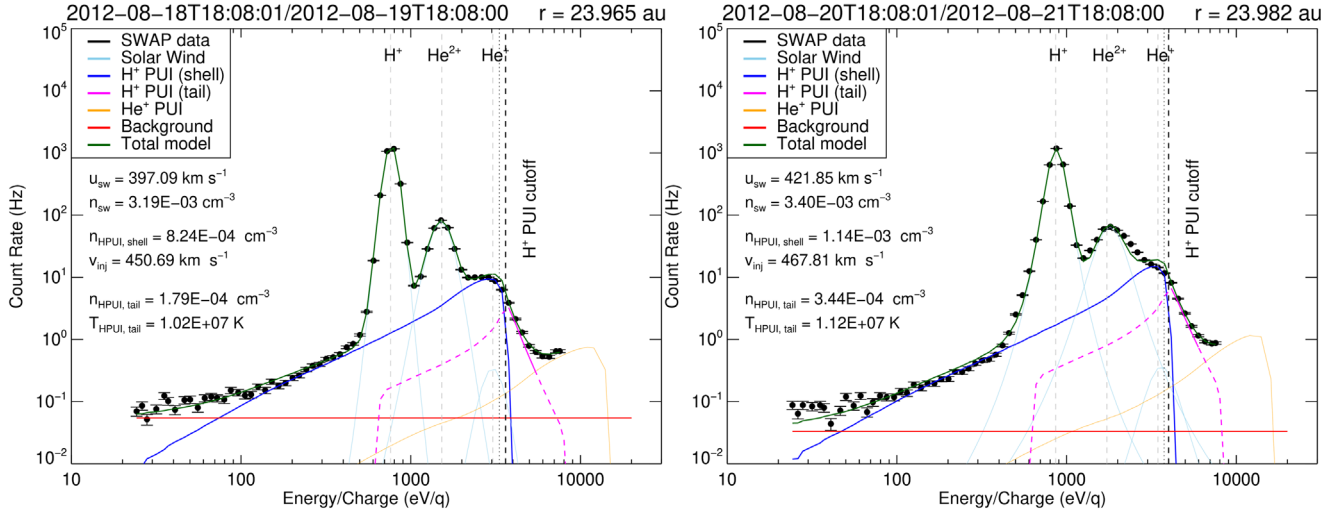


Figure 5. Daily averaged SWAP count rates in the spacecraft frame just before (left panel) and after (right panel) shock S2. The figure has the same notation as in Figures 2 and 3.

suprathermal tails is also affecting the derivation of the cooling index of the shell part of the distribution.

We calculate the shock compression ratio as $r_c = \frac{n_2}{n_1}$, where n_1 and n_2 are the H^+ PUI number density upstream and downstream of the shock, respectively. The upstream and downstream quantities are obtained by averaging them over the shaded regions in Figure 1. As done by Zirnstein et al. (2018) and McComas et al. (2022), we use the H^+ PUI density instead of the H^+ SW density to calculate the shock strength because the H^+ SW density exhibits small-scale fluctuations throughout the shock transition, whereas the PUI properties appear more stable before and after the shock. The erratic behavior of SW density across the shock and the lack of a correlation between SW density and speed makes it difficult to use the SW density measurements to derive the shock jump conditions. However, the PUI density measurements show a clear correlation with the jump in the SW speed, making them useful in deriving shock parameters. We estimate the shock speed (V_{sh}) in the Sun frame as $V_{sh} = \frac{n_2 u_2 - n_1 u_1}{n_2 - n_1}$, where u_1 and u_2 are upstream and downstream SW bulk flow speeds in the Sun frame. Note that a fraction of H^+ PUIs form a suprathermal tail downstream of the shock and the PUI tail density is also included in the calculation of the shock compression ratio and the shock speed. The density compression ratio is 3.19 and the shock speed is 459.1 km s^{-1} in the Sun frame. The compression ratio of this shock is slightly greater than the interplanetary shock analyzed by Zirnstein et al. (2018), making it the strongest interplanetary shock observed in the outer heliosphere by New Horizons SWAP to date.

2.2. Suprathermal H^+ PUI Tail

The H^+ PUI distribution before shock S1 is well represented by a filled-shell distribution (Chen et al. 2014) with a cutoff at approximately twice the bulk SW speed (Figure 2). The underestimation of the count rates in three energy bins around $1.5\text{--}1.8 \text{ keV q}^{-1}$ is because of the presence of heavier solar wind ions; carbon and oxygen (Swaczyna et al. 2019), which is not included in our model of the total SWAP spectrum (solid green line). Also, note that the count rates in these energy bins are not used by McComas et al. (2021) in the fitting of the H^+ PUI filled-shell distribution (solid blue line). On the other hand,

the SWAP histogram downstream of shock S1 shows a tail at energies above the H^+ PUI cutoff (Figure 3), which was not included in the filled-shell distribution fit of McComas et al. (2021). To incorporate the tail in the total H^+ PUI distribution, we fit a power-law distribution to five energy bins above the H^+ PUI cutoff energy (dashed black line in Figure 3). The power-law distribution is assumed to be isotropic in the SW frame such as

$$f(v) = A \left(\frac{v}{v_{inj}} \right)^{-\gamma}, \quad (2)$$

where v is the particle speed in the SW frame, v_{inj} is the H^+ PUI filled-shell cutoff speed in the SW frame, A is a constant term, and γ is the power-law index. The power-law distribution is then converted to the SWAP count rates using Equation (A4) in McComas et al. (2021). Then, a background count rate is added to the model count rates which is taken from the filled-shell distribution fit to the H^+ PUI shell performed by McComas et al. (2021). The χ^2 statistics between the observed and model count rates are minimized by varying A and γ to get the best-fit power-law distribution function. We subtract the modeled H^+ PUI tail count rates from the observed SWAP count rates (black data points) while minimizing the modeled H^+ PUI tail count rates. The model H^+ PUI count rates are obtained by following the procedure in McComas et al. (2021). Note that the conversion to the model count rates uses the correct conversion formula that incorporates the factor $1/2$ as discussed in the appendix in McComas et al. (2021).

The best-fit power-law distribution in the SW frame for the histogram in Figure 3 has the form $f(v) = 3407.9 \left(\frac{v}{v_{inj}} \right)^{-13.2}$ [$s^3 \text{ km}^{-6}$]. The best-fit distribution converted to the model count rates in the instrument frame is shown by the magenta-colored line in Figure 3. The solid and dashed lines represent the model count rates in the fitted and non-fitted energy bins, respectively. Note that it is essential to include the contribution of power-law distribution in energy bins other than the five energy bins used for the fitting when calculating total model count rates (solid green curve), especially to bins just before the

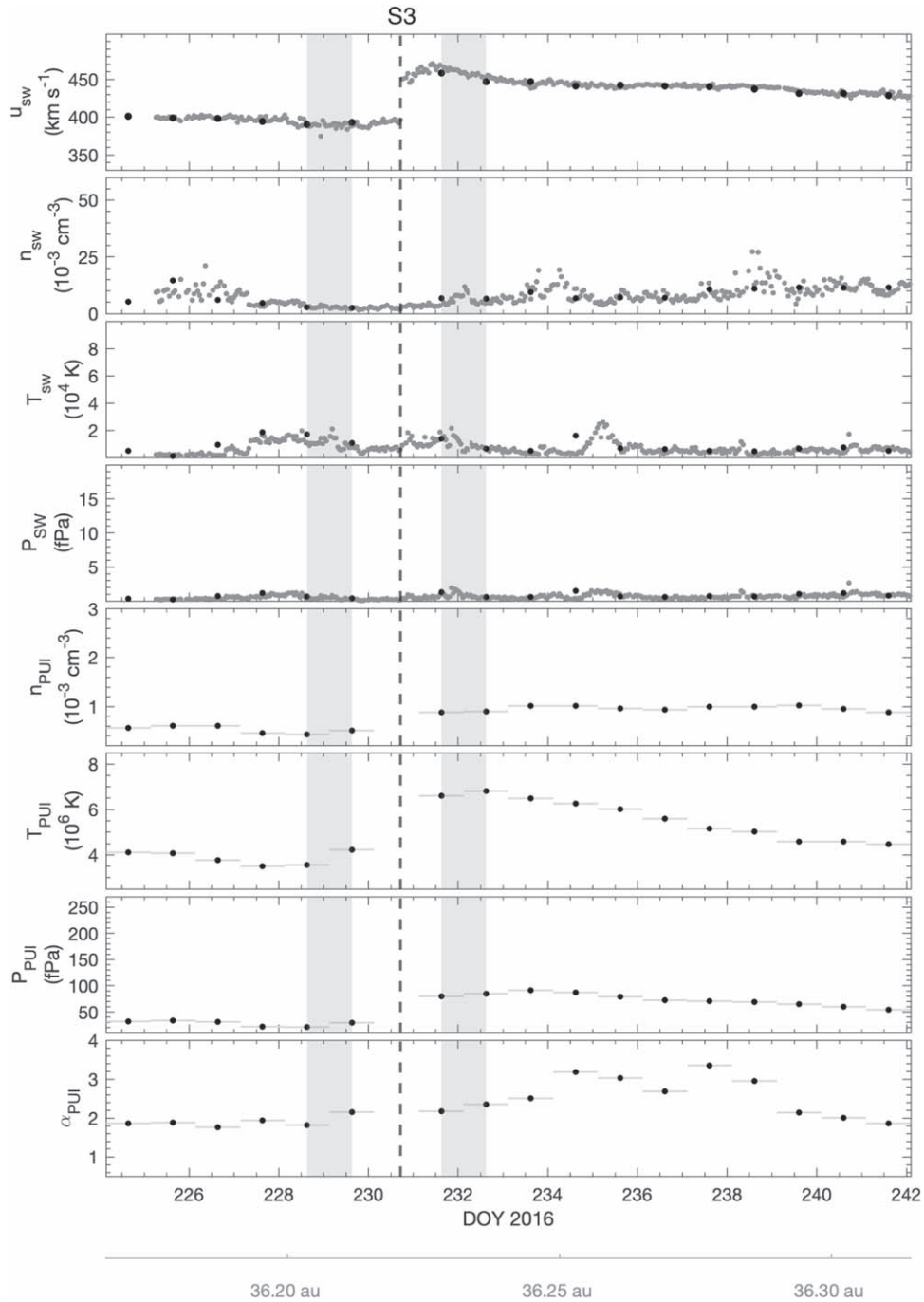


Figure 6. Variation of H^+ SW and H^+ PUI properties across the interplanetary shock S3 observed by SWAP at ~ 36.2 au from the Sun. The figure has the same notation as in Figure 1.

cutoff energy. We derive the density and temperature of the H^+ PUI tail per histogram by integrating the particle distribution obtained from the fitting analysis, i.e., by calculating the distribution moments. Then, the averaged values over the shaded region in Figure 1 are used to compute the downstream quantities. The H^+ PUI tail density downstream of shock S1 is $3.95 \times 10^{-4} \text{ cm}^{-3}$, a significant fraction ($\sim 18.4\%$) of the downstream H^+ PUI density. The effective H^+ PUI tail temperature is $\sim 1.2 \times 10^7 \text{ K}$ in the downstream region, representing evidence of preferential heating of PUIs across the shock. The partial pressure of the H^+ PUI tail is a significant

fraction ($\sim 28\%$) of the overall downstream PUI pressure. The PUI tail persists for ~ 3 days after the shock, where the spectral slope becomes less steep (decreased by $\sim 44\%$) over time before it finally disappears, similar to that strong shock analyzed by Zirnstein et al. (2018). We posit that the disappearance of the PUI tail after ~ 3 days is likely because the SWAP is observing different plasma parcels in the rarefaction region of the fast-forward shock S1, compared to the observation 3 days before. As the shock and the SW are moving very fast compared to New Horizons, this is the most likely case. The adiabatic cooling due to expansion and losses

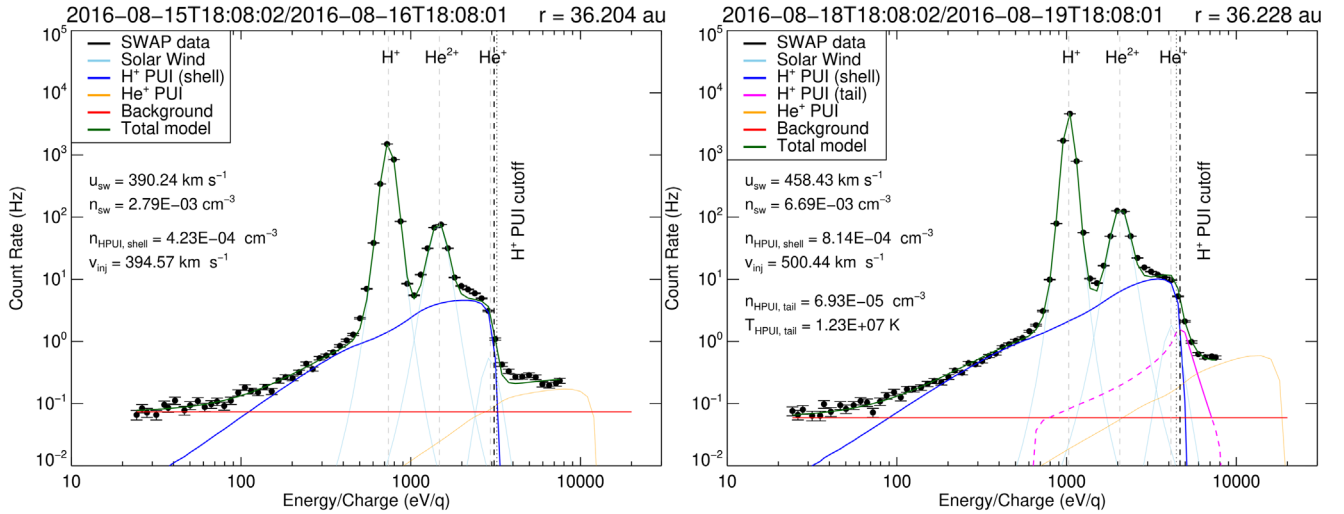


Figure 7. Daily averaged SWAP count rates in the spacecraft frame just before (left panel) and after (right panel) shock S3. The figure has the same notation as in Figures 2 and 3.

due to neutralization in the rarefaction region downstream of the shock can also contribute to the disappearance of the suprathermal PUI tail.

2.3. Other Interplanetary Shocks with a Suprathermal PUI Tail

In this section, we present the analysis of four other shocks that show the signature of a suprathermal tail in the H^+ PUI distribution downstream of the shock. Figure 4 shows the variation of H^+ SW and H^+ PUI properties across a relatively weak interplanetary shock, S2 observed by SWAP at a radial distance of 23.98 au from the Sun. This shock was observed ~ 25 days after shock S1 and was only ~ 0.1 au apart from S1 in the Sun frame during SWAP’s observation. Also, this shock appears to be in the middle of a broad structure with a jump in the H^+ PUI density and temperature ~ 3 –4 days before the shock transition. This broad structure is formed by some unknown physical processes that are beyond the scope of this study.

So, without investigating the physical details regarding the origin of the broad structure, we simply present the analysis of upstream and downstream quantities around the shock. The SW speed shows a very small jump, $\sim 7\%$ from ~ 396.3 km s^{-1} upstream to 423.6 km s^{-1} downstream of the shock (top panel of Figure 4), in the Sun frame. Similar to what was seen in several of the shocks studied by McComas et al. (2022), the H^+ SW density and temperature do not show a clear jump across the shock. Interestingly, we see the presence of a suprathermal H^+ PUI tail in the PUI distribution upstream of the shock as well (left panel of Figure 5). Therefore, we include the contribution of the power-law tail to the H^+ PUI properties across the shock in Figure 4, both upstream and downstream of the shock. The PUI cooling index starts to increase ~ 4 days before the shock, becomes maximum at the shock transition, and goes back to the adiabatic value ~ 7 days after the shock. The estimated shock compression ratio is 1.44 and the shock speed is 485.5 km s^{-1} in the Sun frame. This is the weakest shock in the outer heliosphere showing the signature of a H^+ PUI tail, in the SWAP data, due to the presence of suprathermal H^+ PUI upstream of the shock. The best-fit H^+ PUI tail distribution just after the shock (histogram on the right panel of Figure 5) is represented by $f(v) = 2082.0 \left(\frac{v}{v_{inj}}\right)^{-10.1}$ [s^3 km $^{-6}$].

The downstream histogram shows a very distinct tail with the power-law index of 10.1 which is even less steep compared to shock S1. The power-law index also decreased across the shock from ~ 10.8 to ~ 10.1 . The H^+ PUI tail density downstream of the shock is 2.8×10^{-4} cm $^{-3}$, which is a significant fraction ($\sim 20\%$) of the downstream H^+ PUI density even though the shock compression ratio is very small. The effective H^+ PUI tail temperature in the downwind region is $\sim 1.14 \times 10^7$ K. The partial pressure of the H^+ PUI tail is a significant fraction ($\sim 29\%$) of the overall downstream PUI pressure, even slightly larger than for shock S1.

Figure 6 shows the variation of H^+ SW and H^+ PUI properties across the interplanetary shock S3 observed by SWAP at a heliocentric distance of 36.22 au. The SW speed shows a $\sim 16\%$ jump from ~ 389.4 to 451.7 km s^{-1} downstream of the shock (top panel of Figure 6). The H^+ SW density is increased from 2.69×10^{-3} to 6.63×10^{-3} cm $^{-3}$ but the SW temperature shows erratic behavior without showing an increase in the downstream region (see Table 2). On the other hand, the H^+ PUI density and temperature show a gradual increase across the shock. The estimated shock compression ratio is 1.92 and the shock speed is 519.5 km s^{-1} in the Sun frame. The best-fit H^+ PUI tail distribution for the histogram just after the shock (right panel of Figure 7) is represented by $f(v) = 457.8 \left(\frac{v}{v_{inj}}\right)^{-13.2}$ [s^3 km $^{-6}$]. The H^+ PUI shell consists of most of the PUI density in the downstream region with the H^+ PUI tail contributing $\sim 7.5\%$ ($n_{HPUI,tail} = 6.7 \times 10^{-5}$ cm $^{-3}$) of the total PUI density. The effective H^+ PUI tail temperature is $\sim 1.22 \times 10^7$ K, in the downstream region. The partial pressure of the H^+ PUI tail is a moderate fraction ($\sim 14\%$) of the overall downstream PUI pressure. The H^+ PUI cooling index shows different behavior than for S1 and S2, it increases ~ 4 days after the shock and goes to the original value ~ 9 days after the shock. The behavior of the cooling index across shock S3 is somewhat similar to the results of McComas et al. (2021, 2022).

Figure 8 shows the variation of H^+ SW and H^+ PUI quantities across the interplanetary shock S4 observed by SWAP at a radial distance of 36.67 au from the Sun. The SW speed shows a small jump of $\sim 9.4\%$ from ~ 396.3 km s^{-1} upstream to 433.5 km s^{-1} downstream (top panel of Figure 8) in the Sun frame. The H^+ SW temperature is increased by

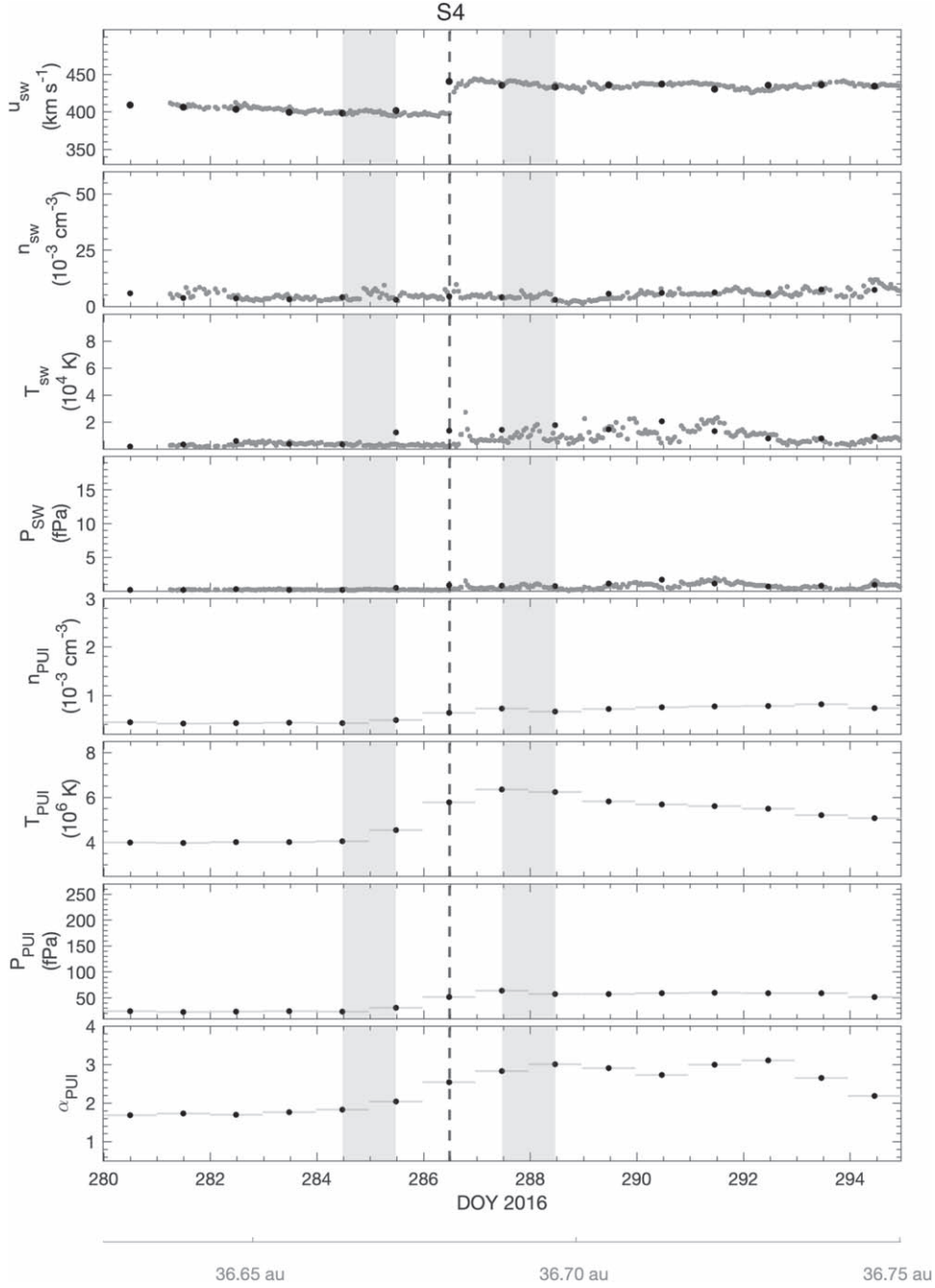


Figure 8. Variation of H^+ SW and H^+ PUI quantities across the interplanetary shock S4 observed by SWAP at ~ 36.7 au from the Sun. The figure has the same notation as in Figure 1.

$\sim 108\%$ from 7.7×10^3 K upstream to 1.6×10^4 K downstream but the SW density again shows behavior unrelated to SW speed across the shock (see Table 2). The H^+ PUI density and temperature show a gradual increase across the shock. The shock compression ratio estimated using the PUI density compression is 1.52 and the shock speed is 504.4 km s^{-1} in the Sun frame. The best-fit H^+ PUI tail distribution for the histogram just after the shock (right panel of Figure 9) is represented by $f(v) = 467.6 \left(\frac{v}{v_{inj}}\right)^{-14.1} [\text{s}^3 \text{ km}^{-6}]$. Again, the H^+ PUI shell consists of most of the PUI density downstream of shock with the H^+ PUI tail contributing $\sim 4.3\%$ ($n_{\text{PUI,tail}} = 3.02 \times 10^{-5} \text{ cm}^{-3}$) of the total H^+ PUI density (see Table 2). The effective H^+ PUI tail temperature in the

downstream region is $\sim 1.16 \times 10^7$ K. The partial pressure of the H^+ PUI tail is a smaller fraction ($\sim 8\%$) of the overall downstream PUI pressure. The cooling index for H^+ PUI increases ~ 2 days before the shock, becomes maximum ~ 6 days after the shock, and then starts to decrease.

Figure 10 shows the variation of H^+ SW and H^+ PUI properties across the interplanetary shock S5 observed by SWAP at a radial distance of 33.59 au from the Sun. This shock has been analyzed before by Zirnstein et al. (2018), using the Vasylunas & Siscoe (1976) model for the PUI shell distribution with the methodology described in McComas et al. (2017). Their analysis did not include (1) the PUI cooling index as a free parameter (Swaczyna et al. 2020; McComas et al.

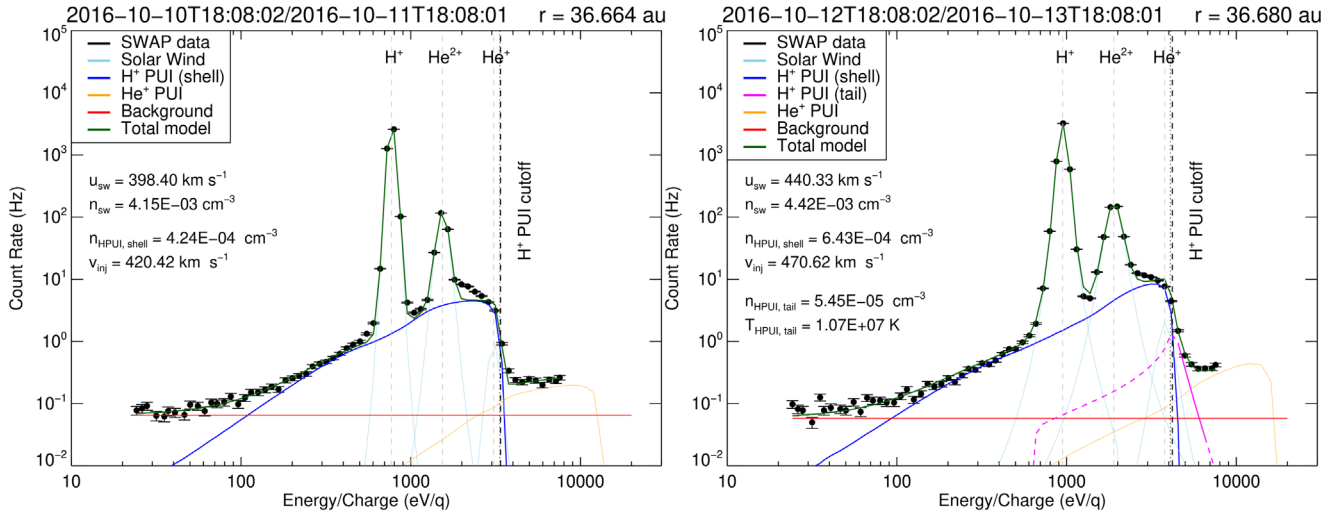


Figure 9. Daily averaged SWAP count rates in the spacecraft frame just before (left panel) and after (right panel) the interplanetary shock S4. The figure has the same notation as in Figures 2 and 3.

2021, 20), and (2) the correct conversion formula for the distribution function to the model count rates (McComas et al. 2021). Therefore, they obtained fitting parameters (ionization rate and the ionization cavity size) for the H^+ PUI shell that will be different to some degree. This also affects the fitting of the H^+ PUI tail and hence the derived PUI quantities across the shock could be different. Our analysis incorporates both improvements in the fitting procedure mentioned above. One significant change in the PUI property obtained from this analysis is that the PUI density is twice that reported by Zirnstein et al. (2018), due to the conversion formula. The SW speed shows a $\sim 20\%$ jump from $\sim 373.3 \text{ km s}^{-1}$ upstream to 447.8 km s^{-1} downstream in the Sun frame (top panel of Figure 10). The H^+ SW temperature shows a $\sim 2000\%$ jump from $1.8 \times 10^3 \text{ K}$ upstream to $3.7 \times 10^4 \text{ K}$ downstream but the SW density again shows erratic behavior across the shock. The H^+ PUI density and temperature show a gradual increase across the shock. The shock compression ratio estimated using the PUI density compression is 2.94 and the shock speed is 486.2 km s^{-1} in the Sun frame. These values are close to that reported by Zirnstein et al. (2018). The best-fit H^+ PUI tail distribution for the histogram immediately after the shock is represented by $f(v) = 1077.8 \left(\frac{v}{v_{inj}}\right)^{-11.2} [\text{s}^3 \text{ km}^{-6}]$. The amplitude (A) and the power-law index (γ) of isotropic H^+ PUI tail distribution downstream of all five shocks are summarized in Table 1. The H^+ PUI tail density downstream of the shock is $3.3 \times 10^{-4} \text{ cm}^{-3}$, which is a significant fraction ($\sim 13.6\%$) of the downstream H^+ PUI density. The effective H^+ PUI tail temperature in the downstream region is $\sim 1.16 \times 10^7 \text{ K}$. The partial pressure of the H^+ PUI tail is a significant fraction ($\sim 25\%$) of the overall downstream PUI pressure. The PUI cooling index shows a gradual increase after the shock until ~ 7 days and then it starts to decrease. This behavior of the cooling index is similar to the finding of McComas et al. (2021).

2.4. Theoretical Estimation of Reflected PUI Number Density

The mechanism of the formation of suprathermal H^+ PUI tail at the distant interplanetary shock is not well understood. A dominant acceleration mechanism at a quasi-perpendicular shock is the reflection of incident ions by the electrostatic CSP.

Table 1
Amplitude and Power-law Index of the Isotropic Power-law Distribution for the H^+ PUI Tail Downstream of the Shocks

Parameters	S1	S2	S3	S4	S5
$A [\text{s}^3 \text{ km}^{-6}]$	3407.9	2082.0	457.8	467.6	1077.8
γ	13.2	10.1	13.2	14.1	11.2

In this section, we investigate if the measurement of the H^+ PUI tail by SWAP is consistent with the theory of acceleration of PUIs by reflection from the electrostatic CSP. For this, we estimate the number density of reflected H^+ PUIs for fast-forward shocks and compare them with SWAP’s observations of the H^+ PUI tail density.

The generalized filled-shell distribution upstream of the distant interplanetary shock can be written in the form of (Chen et al. 2014; Wang et al. 2023)

$$f(v) = \alpha_{\text{PUI}} \frac{n_{\text{PUI}}}{4\pi u_1^{\alpha_{\text{PUI}}}} v^{\alpha_{\text{PUI}}-3} \Theta(u_1 - v), \quad (3)$$

where v is the particle speed in the SW frame, u_1 is the upstream bulk flow speed, n_{PUI} is the PUI number density, α_{PUI} is the PUI cooling index, and $\Theta(u_1 - v)$ is the Heaviside step function. Note that this distribution is a simplified form of the Chen et al. (2014) distribution that excludes the exponential term and is valid for $r \gg \lambda$ (size of ionization cavity). The form of the PUI distribution, Equation (3), avoids the complexity in the calculation of the reflected PUI number density, which includes exponential integral if the Chen et al. (2014) distribution is used, where the integration must be evaluated numerically. As the shocks analyzed in this paper are at a distance far from the ionization cavity, Equation (3) should work very well. Since the interplanetary shocks are moving faster than the SW speed (i.e., fast-forward shock), in the shock frame, the upstream flow approaches the shock at velocity $-V_{\text{sh,sw}}$. In the shock frame, the PUI shell distribution is shifted toward the negative v_x by an amount $-V_{\text{sh,sw}}$ (Figure 12), i.e., the spherical shell is offset from the origin “O” by $-V_{\text{sh,sw}}$. The electrostatic CSP yields a specular reflection speed,

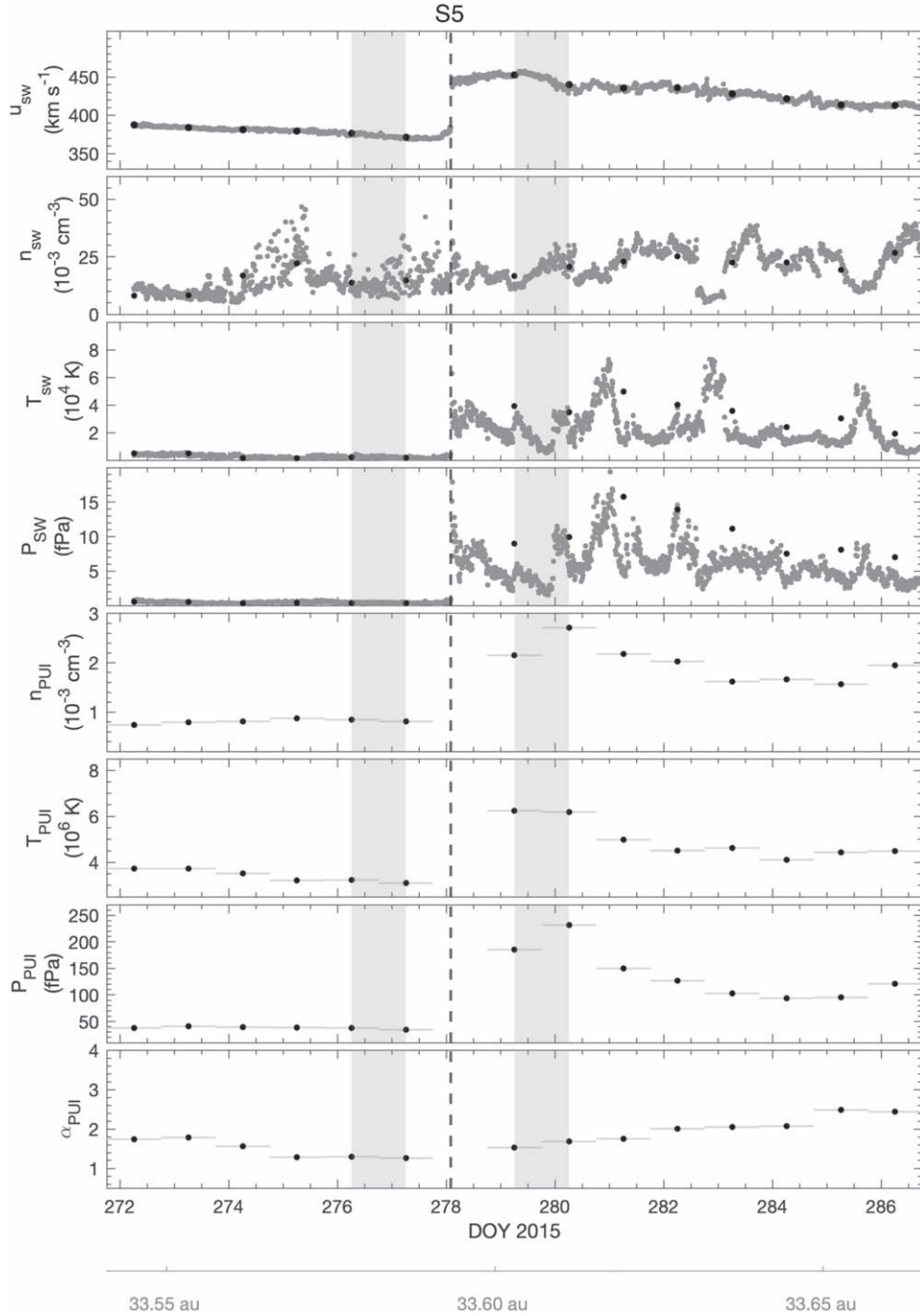


Figure 10. Variation of H^+ SW and H^+ PUI quantities at the interplanetary shock S5 observed by SWAP at ~ 33.6 au from the Sun. The figure has the same notation as in Figure 1.

V_{spec} , which is on the negative side of the origin (marked by a solid vertical green line) and only PUIs with sufficiently large negative v_x (lying on the left of the vertical green line) will push through the CSP. The PUIs to the right of origin will be moving away from the shock because they are moving in the x -direction at a speed faster than the shock. The region between the origin and V_{spec} (shaded green annulus) identifies where the reflected PUIs come from in phase space.

Following the derivation method in Shrestha et al. (2021), we derive the reflected PUI number density (n_{ref}) for a filled-shell distribution of the form Equation (3) for a fast-forward

shock, given by

$$\begin{aligned}
 n_{\text{ref}} = & n_{\text{PUI}} \left[\frac{V_{\text{spec}}}{2u_1} + \frac{1}{2(\alpha_{\text{PUI}} - 1)} \right. \\
 & \times \left\{ \left(\frac{V_{\text{sh,sw}}}{u_1} \right)^{\alpha_{\text{PUI}}} \left(\frac{1}{\left(\frac{V_{\text{sh,sw}}}{u_1} \right)^{\alpha_{\text{PUI}} - 1} - 1} \right) \right. \\
 & \left. \left. \mp \left(\frac{|V_{\text{sh,sw}} - V_{\text{spec}}|}{u_1} \right)^{\alpha_{\text{PUI}}} \left(\frac{1}{\left(\frac{|V_{\text{sh,sw}} - V_{\text{spec}}|}{u_1} \right)^{\alpha_{\text{PUI}} - 1} - 1} \right) \right\} \right], \quad (4)
 \end{aligned}$$

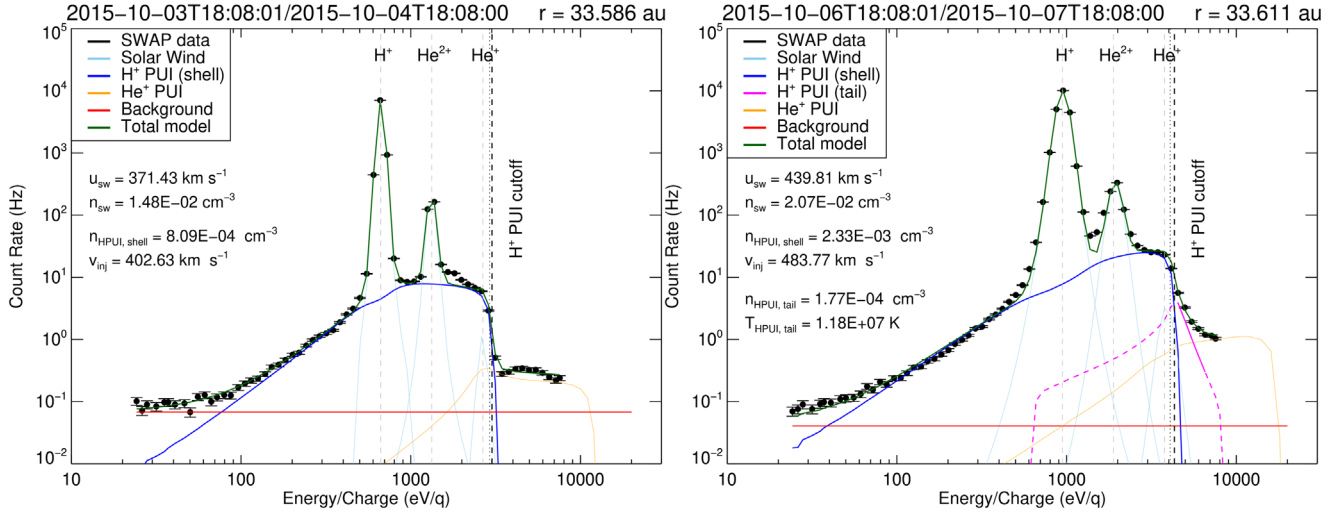


Figure 11. Daily averaged SWAP count rates in the spacecraft frame just before (left panel) and after (right panel) the interplanetary shock S5. The figure has the same notation as in Figures 2 and 3.

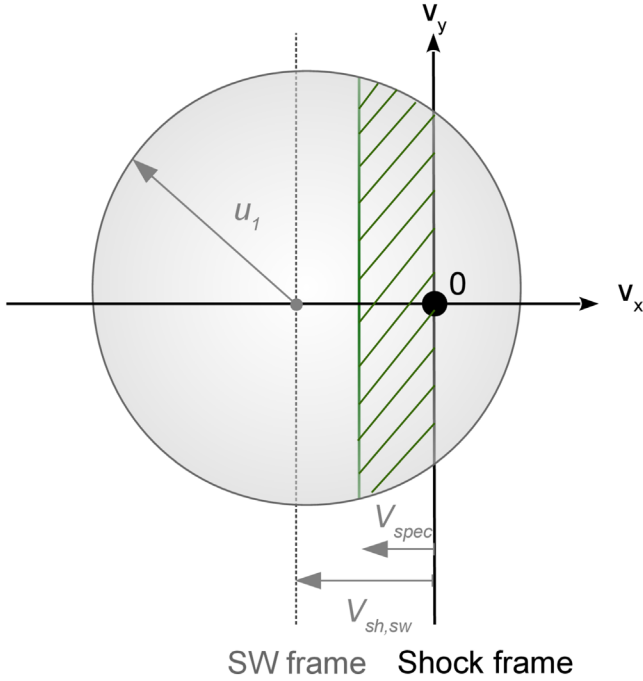


Figure 12. Sketch of the velocity phase-space portrait of a PUI filled-shell distribution in the shock frame just ahead of a fast-forward shock. The dashed line represents the SW frame in which the PUI distribution is isotropic, whereas, in the shock frame centered at “O,” the PUI distribution appears to be shifted by velocity $-V_{sh,sw}$ in the negative v_x . The hatched green region represents where in the velocity phase space the reflected PUIs come from.

where the $-ve$ and $+ve$ signs are for the cases $V_{spec} < V_{sh,sw}$ and $V_{spec} > V_{sh,sw}$, respectively. The specular reflection speed (V_{spec}) is estimated using the electron momentum equation (Leroy 1983; Zank et al. 1996; le Roux et al. 2000),

$$V_{spec}^2 = \frac{2 \eta (r_c - 1)}{M_{A1}^2} u_{1,sh}^2, \quad (5)$$

where η is a scaling factor that accounts for the relative contribution of the magnetic deflection term over the magnetic field compression term on the electrostatic CSP, M_{A1} is the upstream Alfvénic Mach number, and $u_{1,sh}$ is the upstream flow

speed in the shock frame. We assume $\eta = 2$, meaning that the magnetic deflection and magnetic compression term contribute equally to the electrostatic CSP (Quest 1986; Zank et al. 1996). The upstream Alfvén Mach number is given by

$$M_{A1} = \frac{u_{1,sh}}{B_1 / \sqrt{\mu_0 \rho_1}}, \quad (6)$$

where ρ_1 is the upstream plasma density that includes densities of H^+ SW, H^+ PUI, and alpha particles (density of electrons are neglected due to their smaller mass), and B_1 is the magnetic field magnitude at the upstream location of interplanetary shock. Unfortunately, the New Horizons spacecraft is not equipped with a magnetometer, so we do not know the magnetic field direction or magnitude at the time of SWAP observations. Instead, we use Voyager’s much earlier observations of the magnetic field magnitude in the outer heliosphere, as a first-order estimation for the magnetic field that could have existed during the New Horizons crossing. For this, we fit a power law to the Carrington averaged (~ 27 days) Voyager 2 data from ~ 20 – 80 au (black curve on the top panel of Figure 13). The value of the fitted curve (dashed red curve) at each shock location is used as an estimate of the upstream magnetic field magnitude there. The Carrington averaged magnetic field data from Voyager 2 over the distance range of 23.5–37.0 au, however, is highly fluctuating, likely due to SW transient phenomena. To eliminate the effect of fluctuations in the estimated magnetic field magnitude at the shock locations, we fit a power law to the magnetic field magnitude as a function of distance from the Sun and use the fitted value as a first-order estimate of the field to analyze shocks S1–S5. In addition, we find the 16th–84th percentiles of the observed histogram of magnetic field magnitudes over the distance range considered (bottom panel of Figure 13), which we use as an estimate of the 1σ uncertainty in the upstream magnetic field (i.e., assuming a Gaussian distribution, the 16th and 84th percentiles represent 1σ deviations from the mean). A similar range of the magnetic field magnitude over a similar distance range is also considered by Bagenal et al. (2015) and Zirnstein et al. (2018). The power-law fit varies as $r^{-1.03}$, which is expected because at a large distance from the Sun,

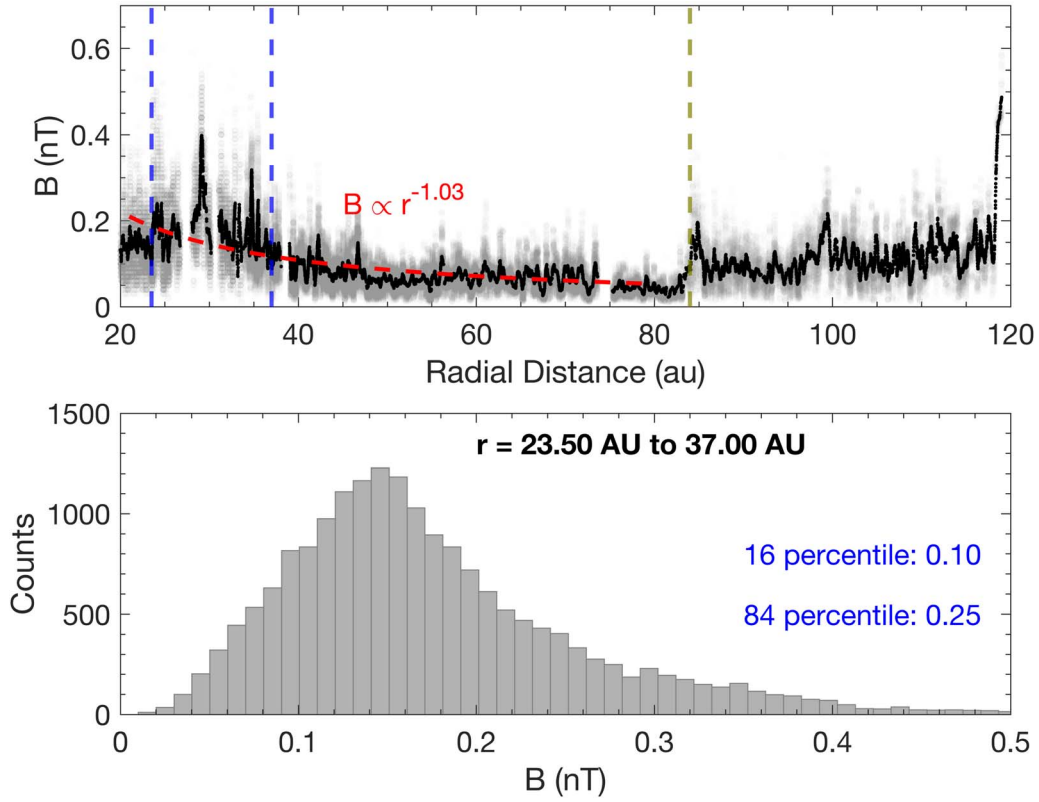


Figure 13. (Top panel) Carrington averaged magnetic field magnitude observed by Voyager 2 from ~ 20 – 120 au (black curve). The gray dots represent individual hourly averaged Voyager 2 data. A power-law fit to the magnetic field from ~ 20 – 80 au is also shown (dashed red line). Two blue vertical dashed lines represent the radial distance from the Sun for SWAP data used in this study (~ 23.5 – 37.0 au). The olive-colored vertical dashed line represents the location of HTS. (Bottom panel) Histogram of the magnetic field magnitude from 23.5–37.0 au. The magnetic field’s 16th and 84th percentile values are shown in blue text.

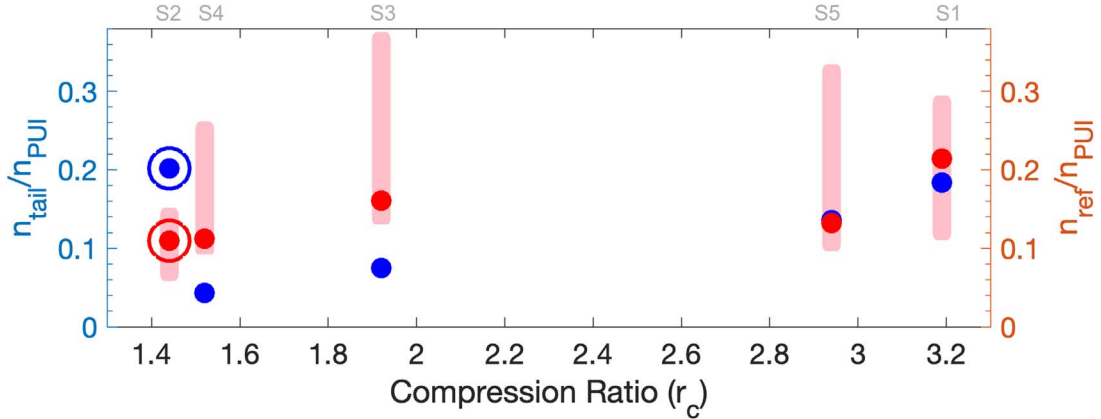


Figure 14. Variation of the observed H^+ PUI tail number density fraction (filled blue circle) with the shock compression ratio. The variation of reflected H^+ PUI density fraction from the theory of electrostatic CSP (filled red circle) and its possible range based on the 16th–84th percentile value of the magnetic field magnitude over 23.5–37.0 au is also shown (red area around the red circle).

the magnetic field is mostly transverse, and the transverse magnetic field varies as r^{-1} according to Parker’s spiral field theory (Parker 1961). We also assume that the shocks are perpendicular, for simplicity, which is a reasonable assumption over the distance considered in this study.

The reflected H^+ PUI number density fraction estimated using Equation (4) for all five shocks discussed before as a function of compression ratio is shown in Figure 14 (filled red circle). A possible range of the reflected H^+ PUI number density fraction calculated based on the 16th–84th percentiles of the magnetic field values over the distance range of

23.5–37.0 au is shown by the red area around the red circles. The large range for the theoretically estimated value is because of a larger spread in the magnetic field observed by Voyager 2 that ranges from 0.10 nT (16 percentile) to 0.25 nT (84 percentile). The asymmetric range for reflected PUI density fraction is because of an asymmetric distribution of magnetic field over 23.5–37.0 au (see bottom panel of Figure 13). The H^+ PUI tail density calculated from the SWAP observations is overplotted on the same figure (filled blue circle) for easier comparison with the theoretical estimation. The densities of the H^+ PUI tail and reflected H^+ PUIs are summarized in Table 2.

Table 2
Shock Parameters for All Five Shocks Analyzed in This Paper

Parameters	S1		S2		S3		S4		S5	
	Upstream	Downstream	Upstream	Downstream	Upstream	Downstream	Upstream	Downstream	Upstream	Downstream
Bulk flow speed [km s ⁻¹] ^a	107.6	33.8	89.2	61.9	130.1	67.8	108.1	70.9	112.8	38.4
H ⁺ SW density [cm ⁻³]	1.05×10^{-2}	1.10×10^{-2}	4.83×10^{-3}	4.40×10^{-3}	2.69×10^{-3}	6.63×10^{-3}	3.53×10^{-3}	3.55×10^{-3}	1.43×10^{-2}	1.87×10^{-2}
H ⁺ PUI shell density [cm ⁻³]	6.76×10^{-4}	1.76×10^{-3}	9.62×10^{-4}	1.22×10^{-3}	4.63×10^{-4}	8.21×10^{-4}	4.57×10^{-4}	6.66×10^{-4}	8.26×10^{-4}	2.1×10^{-3}
H ⁺ PUI tail density [cm ⁻³]	...	3.95×10^{-4}	2.13×10^{-4}	2.80×10^{-4}	...	6.68×10^{-5}	...	3.02×10^{-5}	...	3.30×10^{-4}
H ⁺ SW temperature [K]	1.7×10^4	4.4×10^4	3.2×10^4	4.0×10^4	1.4×10^4	1.0×10^4	7.7×10^3	1.6×10^4	1.8×10^3	3.7×10^4
H ⁺ PUI shell temperature [K]	3.8×10^6	7.1×10^6	5.8×10^6	6.4×10^6	3.9×10^6	6.3×10^6	4.3×10^6	6.1×10^6	3.2×10^6	5.4×10^6
H ⁺ PUI tail temperature [K]	...	1.20×10^7	1.02×10^7	1.14×10^7	...	1.22×10^7	...	1.16×10^7	...	1.16×10^7
Magnetic field magnitude [nT] ^b	0.19	0.61	0.18	0.26	0.12	0.23	0.12	0.18	0.13	0.38
Alfvén speed [km s ⁻¹]	33.5	104.8	46.1	65.6	42.3	54.7	38.2	55.3	22.1	53.2
Sonic Mach #	2.1	0.3	1.1	0.6	1.7	0.7	1.5	0.7	2.5	0.4
Fast magnetosonic Mach #	1.8	0.2	0.9 ^c	0.5	1.5	0.6	1.3	0.6	2.3	0.4
Alfvén Mach #	3.2	0.3	1.9	0.9	3.1	1.2	2.8	1.3	5.1	0.7
Compression ratio (r_c)		3.19		1.44		1.92		1.52		2.94
Shock speed [km s ⁻¹]		495.1		485.5		519.5		504.4		486.2
V_{spec} [km s ⁻¹]		99.0		61.2		81.2		55.4		61.8
$\frac{n_{\text{tail}}}{n_{\text{PUI}}}$		0.184		0.202		0.075		0.043		0.136
$\frac{n_{\text{ref,d}}}{n_{\text{PUI}}}$		$0.214 \begin{pmatrix} +0.080 \\ -0.103 \end{pmatrix}$		$0.110 \begin{pmatrix} +0.041 \\ -0.051 \end{pmatrix}$		$0.161 \begin{pmatrix} +0.214 \\ -0.030 \end{pmatrix}$		$0.112 \begin{pmatrix} +0.149 \\ -0.019 \end{pmatrix}$		$0.132 \begin{pmatrix} +0.202 \\ -0.035 \end{pmatrix}$

Notes. Note that the fast magnetosonic Mach number is close to the sonic Mach number because the PUI thermal pressure is much larger than the magnetic pressure.

^a The bulk flow speed is in the shock frame.

^b The Magnetic field magnitude upstream of the shock is obtained from the power-law fit of the Voyager 2 data and the value in the downstream region is obtained by assuming a perpendicular shock, i.e., $B_2 = r_c B_1$.

^c Shock S2 has a fast magnetosonic Mach number less than 1 meaning that this shock may have already been modified into a compression wave.

^d The values with – and + signs represent a possible range of reflected H⁺ PUI density fraction based on the 16 and 84 percentiles of the magnetic field over 23.7–36.8 au.

Interestingly, the match between the observed and theoretical values is very good for the two interplanetary shocks with higher compression ratios ($r_c \geq 2.9$, S1, and S5). A good match suggests that the suprathermal H^+ PUI tail in the SWAP energy range for stronger shocks is consistent with the idea of the formation of a PUI tail by reflection from the electrostatic CSP. On the other hand, the match is poor for the three interplanetary shocks with lower compression ratios ($r_c \leq 2$). In addition, the theory predicts a higher reflected number density fraction for shocks S3 and S4, whereas the theoretical estimate is lower for shock S2. The lower theoretical estimate for shock S2 is likely due to additional physical processes, such as SDA, DSA, reflection from magnetic deflection, reflection in contracting and reconnecting magnetic islands, etc. The higher theoretical estimate for shocks S3 and S4 may indicate that the H^+ PUI tail in the SWAP energy range for these shocks can be formed by physical processes other than the reflection from electrostatic CSP.

At last, the SWAP observations show that the density fraction of the H^+ PUI tail increases with the shock compression ratio, except for shock S2. This is clear from Equation (4), which shows that the reflected PUI number density is proportional to the V_{spec} , and hence, the shock compression ratio. A similar pattern in the variation of reflected H^+ PUI number density with the shock strength is observed from the theoretical estimate. As mentioned before, the H^+ PUI tail for shock S2 may have contributions from other physical processes and they do not appear to follow the expected trends of variation with the shock compression.

3. Summary and Conclusions

We have presented a detailed analysis of five fast-forward interplanetary shocks that exhibit the signature of a suprathermal tail in the H^+ PUI distribution downstream of the shock. These shocks were observed by New Horizons' SWAP at ~ 24 hr PUI data cadence at the heliocentric distances ranging from 23.7–36.8 au. The estimated shock compression ratios range from ~ 1.4 – 3.2 , with shock S1 being the strongest interplanetary shock observed by SWAP so far in the outer heliosphere, and shock S2 being the weakest shock that still shows the signature of a H^+ PUI tail. Shock S2 appears to be situated within a broad structure. In general, the H^+ SW density displays erratic behavior across the shocks without showing a clear compression downstream. Conversely, the H^+ PUI density exhibits a gradual increase across the shock, allowing us to compute the shock compression ratio. The variation of the H^+ PUI cooling index across the shock showed no consistent pattern among the five shocks. This finding is somewhat inconsistent with the results of McComas et al. (2022) where the enhancement in the PUI cooling index occurred only ~ 1 – 2 weeks after the shock. The different behavior of the PUI cooling index is likely related to the presence of a suprathermal PUI tail in the downstream H^+ PUI distribution. The shock parameters, as well as both upstream and downstream shock quantities for all five shocks, are summarized in Table 2.



The H^+ PUI tail density, determined by fitting an isotropic power-law distribution in the SW frame, is found to be very close to the theoretical estimate based on the theory of PUI reflection from the electrostatic CSP, for stronger shocks ($r_c \geq 2.9$). This finding shows the consistency between the observed H^+ PUI tail in the SWAP energy range and the theory of electrostatic CSP for stronger shocks, though the uncertainty

of the theoretical estimate is large because of the uncertainty in the estimation of the magnetic field magnitude at the upstream shock locations. However, for weaker shocks, the theoretical estimates are larger than the observed values, except for shock S2. The higher estimate for weaker shocks suggests that the H^+ PUI tail in the SWAP energy range for these shocks may not have formed solely due to ion reflection from the electrostatic CSP. The smaller theoretical estimate for shock S2 likely results from the contribution of other physical processes in accelerating PUIs, in addition to the electrostatic CSP. Additionally, this study suggests, for the first time, that the observed suprathermal H^+ PUI tail density ratio in the SWAP energy range increases with the strength of the shock, except for shock S2 which appears to be a unique case that should be studied further.

Acknowledgments

This work is supported by the New Horizons mission (M99023MJM; PU-AWD1006357) as part of NASA's New Frontier program. B.S., E.Z., and D.M. also acknowledge support from the IBEX mission (80NSSC20K0719) as part of NASA's Explorer Program. The data used in this study come from McComas et al. (2021) study and are publicly available at https://spacephysics.princeton.edu/sites/g/files/toruqf1376/files/media/swap_pui_data_1.txt and <https://cdaweb.gsfc.nasa.gov/>. The Voyager 2 magnetic field data are publicly available at <https://cdaweb.gsfc.nasa.gov/>. B.S. thanks Pawel Swaczyna and Gary P. Zank for the helpful discussions.

ORCID iDs

Bishwas L. Shrestha  <https://orcid.org/0000-0002-5247-4107>
 Eric J. Zirnstein  <https://orcid.org/0000-0001-7240-0618>
 David J. McComas  <https://orcid.org/0000-0001-6160-1158>
 Pontus Brandt  <https://orcid.org/0000-0002-4644-0306>
 Alan Stern  <https://orcid.org/0000-0001-5018-7537>
 Heather A. Elliott  <https://orcid.org/0000-0003-2297-3922>
 Andrew R. Poppe  <https://orcid.org/0000-0001-8137-8176>
 Kelsi N. Singer  <https://orcid.org/0000-0003-3045-8445>
 Anne Verbiscer  <https://orcid.org/0000-0002-3323-9304>

References

- Bagenal, F., Delamere, P. A., Elliott, H. A., et al. 2015, *JGRE*, 120, 1497
 Baliukin, I. I., Izmodenov, V. V., & Alexashov, D. B. 2022, *MNRAS*, 509, 5437
 Bzowski, M., Möbius, E., Tarnopolski, S., Izmodenov, V., & Gloeckler, G. 2009, *SSRv*, 143, 177
 Chen, J. H., Bochsler, P., Möbius, E., & Gloeckler, G. 2014, *JGRA*, 119, 7142
 Decker, R. B., Krimigis, S. M., Roelof, E. C., et al. 2008, *Natur*, 454, 67
 Dialynas, K., Galli, A., Dayeh, M. A., et al. 2020, *ApJL*, 905, L24
 Drake, J. F., Swisdak, M., & Fermo, R. 2013, *ApJL*, 763, L5
 Gialalone, J. 2012, *ApJ*, 761, 28
 Gialalone, J., Fahr, H., Fichtner, H., et al. 2022, *SSRv*, 218, 22
 Gialalone, J., & Jokipii, J. R. 1999, *ApJ*, 520, 204
 Gkioulidou, M., Opher, M., Kornbleuth, M., et al. 2022, *ApJL*, 931, L21
 Isenberg, P. A. 1986, *JGR*, 91, 9965
 Kornbleuth, M., Opher, M., Zank, G. P., et al. 2023, *ApJL*, 944, L47
 Krimigis, S. M., Mitchell, D. G., Roelof, E. C., Hsieh, K. C., & McComas, D. J. 2009, *Sci*, 326, 971
 Kumar, R., Zirnstein, E. J., & Spitkovsky, A. 2018, *ApJ*, 860, 156
 Le Roux, J. A., & Ptuskin, V. S. 1998, *JGR*, 103, 4799
 le Roux, J. A., Zank, G. P., Fichtner, H., & Ptuskin, V. S. 2000, *GeoRL*, 27, 2873
 Lee, M. A., Mewaldt, R. A., & Gialalone, J. 2012, *SSRv*, 173, 247
 Lee, M. A., Shapiro, V. D., & Sagdeev, R. Z. 1996, *JGR*, 101, 4777

- Leroy, M. M. 1983, [PhFI](#), **26**, 2742
- Lipatov, A. S., Zank, G. P., & Pauls, H. L. 1998, [JGR](#), **103**, 29679
- McComas, D., Allegrini, F., Bagenal, F., et al. 2008, [SSRv](#), **140**, 261
- McComas, D. J., Allegrini, F., Bochsler, P., et al. 2009, [Sci](#), **326**, 959
- McComas, D. J., Shrestha, B. L., Swaczyna, P., et al. 2022, [ApJ](#), **934**, 147
- McComas, D. J., Swaczyna, P., Szalay, J. R., et al. 2021, [ApJS](#), **254**, 19
- McComas, D. J., Zirnstein, E. J., Bzowski, M., et al. 2017, [ApJS](#), **233**, 8
- Mostafavi, P., Zank, G. P., & Webb, G. M. 2018, [ApJ](#), **868**, 120
- Parker, E. N. 1961, [ApJ](#), **134**, 20
- Perri, S., Bykov, A., Fahr, H., Fichtner, H., & Giacalone, J. 2022, [SSRv](#), **218**, 26
- Quest, K. B. 1986, [JGR](#), **91**, 8805
- Randol, B. M., Elliott, H. A., Gosling, J. T., McComas, D. J., & Schwadron, N. A. 2012, [ApJ](#), **755**, 75
- Randol, B. M., McComas, D. J., & Schwadron, N. A. 2013, [ApJ](#), **768**, 120
- Rice, W. K. M., Zank, G. P., le Roux, J. A., & Matthaeus, W. H. 2001, [AdSpR](#), **27**, 835
- Richardson, J. D., Liu, Y., & Wang, C. 2008, [AdSpR](#), **41**, 237
- Shrestha, B. L., Zirnstein, E. J., & Heerikhuisen, J. 2020, [ApJ](#), **894**, 102
- Shrestha, B. L., Zirnstein, E. J., Heerikhuisen, J., & Zank, G. P. 2021, [ApJS](#), **254**, 32
- Swaczyna, P., McComas, D. J., & Zirnstein, E. J. 2019, [ApJ](#), **875**, 36
- Swaczyna, P., McComas, D. J., Zirnstein, E. J., et al. 2020, [ApJ](#), **903**, 48
- Vasyliunas, V. M., & Siscoe, G. L. 1976, [JGR](#), **81**, 1247
- Wang, B., Zank, G. P., Shrestha, B. L., Kombleuth, M., & Opher, M. 2023, [ApJ](#), **944**, 198
- Zank, G. P. 2014, *Transport Processes in Space Physics and Astrophysics*, Vol. 877 (Berlin: Springer)
- Zank, G. P., Heerikhuisen, J., Pogorelov, N. V., Burrows, R., & McComas, D. 2010, [ApJ](#), **708**, 1092
- Zank, G. P., Li, G., Florinski, V., et al. 2006, [JGRA](#), **111**, A06108
- Zank, G. P., Pauls, H. L., Cairns, I. H., & Webb, G. M. 1996, [JGR](#), **101**, 457
- Zank, G. P., Rice, W. K. M., le Roux, J. A., Cairns, I. H., & Webb, G. M. 2001, [PhPI](#), **8**, 4560
- Zirnstein, E. J., Kumar, R., Bandyopadhyay, R., et al. 2021, [ApJL](#), **916**, L21
- Zirnstein, E. J., McComas, D. J., Kumar, R., et al. 2018, [PhRvL](#), **121**, 075102
- Zirnstein, E. J., Möbius, E., Zhang, M., et al. 2022, [SSRv](#), **218**, 28